

Tensor recovery from binary measurements fused low-rankness and smoothness

Jingyao Hou^{a,*}, Xinling Liu^a, Hailin Wang^b, Ke Guo^a

^a Key Laboratory of Optimization Theory and Applications at China West Normal University of Sichuan Province, School of Mathematics and Information, China West Normal University, Nanchong 637009, China

^b School of Mathematics and Statistics, Xi'an Jiaotong University, Xi'an 710049, China

ARTICLE INFO

Keywords:

Binary measurements
Tensor recovery
Low-rankness
Smoothness
ADMM

ABSTRACT

Tensor compressed sensing (TCS) from binary measurements aims to recover a tensor with low-rankness from the binary quantization of its degraded linear measurements, which inherits the advantages of low equipment cost and high sampling efficiency of coarse quantization. Recently, numerous studies have demonstrated that incorporating the properties of low-rankness and local smoothness, which are commonly observed in practical tensor data, can significantly enhance conventional tensor recovery tasks. This motivates us to utilize the low-rank and smooth properties in solving TCS problems from binary measurements. Equipped with the recently proposed tensor correlated total variation (TCTV) that simultaneously regularizes low-rankness and smoothness, we present a regularized model for this problem in this paper. We rigorously prove the recovery guarantee for the proposed model and provide an explicit selection rule for the regularization parameter. Moreover, the theoretical results demonstrate the robustness of the proposed method against both bit flips and pre-quantization noises. An algorithm based on alternating direction multiplier method (ADMM) is presented for solving the proposed model, with its global convergence been proven. Finally, a series of experiments demonstrate the superior performance of our method compared to many other competing approaches.

1. Introduction

Ever since the pioneering work of compressed sensing (CS) [1], it has garnered significant attention and found widespread applications. Mathematically, CS involves obtaining infinite-precision real-valued measurement $y = \Phi x$ of a sparse signal $x \in \mathbb{R}^n$ via a measurement matrix $\Phi \in \mathbb{R}^{m \times n}$ satisfying $m \ll n$. Apparently, the model is inherently limited to unquantized observations, which fails to account for the ubiquitous quantization process involved in real-world applications. Quantization is a process that maps signals into bitstreams and is an essential step prior to storage, processing, and transmission. It has been observed that as resolution increases linearly, there is an exponential rise in power consumption, manufacturing cost, and chip area for analog-to-digital devices employed in signal processing [2]. Consequently, in certain large-scale machine learning or signal processing systems, it is advantageous to operate with coarsely quantized data, particularly employing the most extreme binary (one-bit) data. For instance, in the domain of contemporary machine learning, extensive datasets and intricate models are pervasive, necessitating the adoption of distributed learning systems [3] that often involve frequent communication among multiple computational nodes. In scenarios where

internet connections are slow or unstable (e.g., low-power or low-bandwidth devices such as mobile devices), it would be impractical to work with data at high precision (due to the prohibitive communication cost or power consumption). However, employing coarse quantization has proven effective in overcoming this bottleneck (e.g., [4]). Due to the pervasive demand for coarse quantization, one-bit CS was proposed [5] and has since garnered significant attention [2,6–8]. As a novel paradigm of CS, one-bit CS only stores the signs of real-valued measurements $y = \Phi x$, i.e., $y = \text{sign}(\Phi x) \in \{-1, 1\}^m$ where $\text{sign}(\cdot)$ is defined by $\text{sign}(v) = 1$ if $v \geq 0$ and -1 otherwise, and still hopes to recover the normalized signal $x/\|x\|_2$.¹ For further applications of one-bit CS in multiple-input multiple-output systems (MIMO) and wireless sensor networks, please refer to [9,10].

Besides, data structures are becoming increasingly intricate in various fields, surpassing the scope of sparse vectors. Matrices are commonly used to represent grey images and film ratings. Multidimensional arrays, also known as tensors [11], naturally depict color images, hyperspectral images (HSIs) [12], video sequences [13,14], and magnetic resonance imaging (MRI) data [15]. As one-bit CS is designed for vector

* Corresponding author.

E-mail address: hjy17623226280@163.com (J. Hou).

¹ The scale (absolute amplitude) of the tensor is lost during the binary quantization process. Thus we restrict our attention to tensors on the unit sphere.

data, it requires the vectorization of matrix and tensor data to conform to its operational paradigm. However, this process inevitably results in the loss of some underlying structural information, which may hinder the effectiveness of one-bit CS. To address this issue, a more preferable approach would be to directly conduct CS on primordial matrix/tensor data based on its binary measurements. Building upon this notion, Foucart and Lynch [16] proposed and investigated the problem of matrix CS from binary measurements, i.e., recovering the underlying matrix $\mathbf{X} \in \mathbb{R}^{n_1 \times n_2}$ from

$$\mathbf{y} = \text{sign}(\mathcal{M}(\mathbf{X})) \in \{-1, 1\}^m, \quad (1)$$

where $\mathcal{M} \in \mathbb{R}^{n_1 \times n_2} \rightarrow \mathbb{R}^m$ is a linear operator such that $(\mathcal{M}(\mathbf{X}))_i = \langle \mathbf{A}_i, \mathbf{X} \rangle$ ($i \in [m]$), with \mathbf{A}_i ($i \in [m]$) being independent sensing matrices populated by independent standard Gaussian random variables. Furthermore, our previous research [17] introduced and investigated the problem of tensor CS (TCS) from binary measurements. Specifically, we aim to recover the underlying tensor $\mathcal{X} \in \mathbb{R}^{n_1 \times n_2 \times n_3}$ from

$$\mathbf{y} = \text{sign}(\mathfrak{M}(\mathcal{X})) \in \{-1, 1\}^m, \quad (2)$$

where $\mathfrak{M} \in \mathbb{R}^{n_1 \times n_2 \times n_3} \rightarrow \mathbb{R}^m$ is a linear operator defined as $(\mathfrak{M}(\mathcal{X}))_i = \langle \mathbf{A}_i, \mathcal{X} \rangle$ ($i \in [m]$), with \mathbf{A}_i ($i \in [m]$) being independent sensing tensors populated by independent standard Gaussian random variables. The measurement models (1) and (2) encounter the challenge of ill-conditioning due to insufficient measurements and extreme quantization. To deal with it, enlightened by the sparse assumption in one-bit CS, the above works are built on the premise that the intrinsic dimension of underlying data is significantly lower than its environmental dimension.

More specifically, Foucart and Lynch [16] considered matrices of low-rank, and our previous work [17] required the underlying needed-to-be-recovered tensor to possess low-rankness under the framework of tensor singular value decomposition (T-SVD) [18]. Low-rankness is a prior property that characterizes the global-scale information correlation along this tensor mode, which is widely present in real-world datasets. For instance, the nonlocal self-similarity of natural images implies that the matrices formed by their nonlocal similar patches are low-rank [19,20]; HSIs and MSIs exhibit low-rankness in their spectral space [21]. With the low-rank assumption, we have demonstrated in [17] that the underlying tensor can be reconstructed by solving

$$\min \|\mathcal{M}\|_{\star_L} \quad \text{s.t.} \quad \mathbf{y} = \text{sign}(\mathfrak{M}(\mathcal{M})), \quad \|\mathcal{M}\|_F = 1, \quad (3)$$

where the tensor nuclear norm (TNN) $\|\cdot\|_{\star_L}$ (see Definition 2.8) is a convex relaxation of tensor tubal rank (see Definition 2.6). Due to the nonconvex constraint $\|\mathcal{M}\|_F = 1$, efficiently tackling (3) is challenging. Therefore, in our previous work [22], we turn to the following convex regularized model

$$\min_{\|\mathcal{M}\|_F \leq 1} -\frac{1}{m} \sum_{i=1}^m y_i \langle \mathbf{A}_i, \mathcal{M} \rangle + \lambda_{\text{TNN}} \|\mathcal{M}\|_{\star_L}, \quad (4)$$

where λ_{TNN} denotes a regularization parameter. As demonstrated in [22], the closed-form solution for (4) can be expressed as

$$\hat{\mathcal{X}} = \frac{D_{\lambda_{\text{TNN}}}(\frac{1}{m} \sum_{i=1}^m y_i \mathbf{A}_i)}{\|D_{\lambda_{\text{TNN}}}(\frac{1}{m} \sum_{i=1}^m y_i \mathbf{A}_i)\|_F}, \quad (5)$$

where $D_{\lambda_{\text{TNN}}}(\cdot)$ denotes the tensor singular value thresholding (T-SVT) operator defined in [12] for discrete Fourier transform (DFT) based T-SVD and in [23] for any invertible linear transforms based T-SVD. One-bit low-rank tensor completion (LRTC) [24–26] also aims to recover the underlying tensor from incomplete sign observations. In the one-bit LRTC problem, the underlying low-rank tensor $\mathcal{X} \in \mathbb{R}^{n_1 \times n_2 \times n_3}$ is observed via

$$\mathcal{Y}_{ijk} = \begin{cases} +1, & \text{if } \mathcal{X}_{ijk} + \mathcal{Z}_{ijk} \geq 0 \\ -1, & \text{if } \mathcal{X}_{ijk} + \mathcal{Z}_{ijk} < 0 \end{cases} \quad (i, j, k) \in \Omega, \quad (6)$$

where $\Omega \subset [n_1] \times [n_2] \times [n_3]$ is an index set and \mathcal{Z} denotes a noise tensor consisting of i.i.d random variables. In the observation model

(6), the noise tensor \mathcal{Z} serves as dithering, and it is necessary for us to have knowledge of differentiable distribution functions of noises. It can be observed that the observations differ significantly from binary measurements in TCS problems.

Although the low-rank property is prominent, real-world data possess numerous other significant prior properties. For instance, local smoothness is a commonly used assumption in visual data recovery tasks as it reflects a fundamental structural property of practical visual data. Specifically, adjacent pixels in visual data tend to exhibit continuity in their values, which leads to sparsity in the gradient transformation of the original image through the use of first-order differential operators. The sparsity of gradient maps can be naturally represented by total variation (TV) (see Section 2.3) regularization, along with various modes of primordial data. Therefore, TV regularization modeling has attracted significant interest from researchers. For instance, Cai and Xu [27] have proved that the TV minimization model can be applied to the CS of gradient-sparse signal $\mathbf{x} \in \mathbb{R}^n$. Needell and Ward have employed the TV minimization model for CS of matrices [28] and tensors [29] which possess local smoothness. In [22], we apply the TV minimization method to reconstruct a locally smooth tensor $\mathcal{X} \in \mathbb{R}^{n_1 \times n_2 \times n_3}$ from binary measurements (2) by solving the following model

$$\min_{\|\mathcal{M}\|_F \leq 1} -\frac{1}{m} \sum_{i=1}^m y_i \langle \mathbf{A}_i, \mathcal{M} \rangle + \lambda_{\text{TV}} \|\mathcal{M}\|_{\text{TV}}, \quad (7)$$

where the regularization parameter λ_{TV} equals

$c \sqrt{\frac{(n_{(1)}+2/\pi)n_{(2)}n_3 \log((n_1+n_2)n_3)}{m}}$ with c as a proper constant, $n_{(1)} = \max\{n_1, n_2\}$, and $n_{(2)} = \min\{n_1, n_2\}$. By using auxiliary variables, model (7) can be solved by alternating direction multiplier method (ADMM) [22].

In real applications, the encountered data are usually both low-rank and locally smooth simultaneously. Typical examples include HSIs, MSIs, and MRI images mentioned above. To illustrate this point clearly, we randomly select one HSI dataset, HYDICE Urbanpart, to illustrate this phenomenon. As shown in Fig. 1, column (a) shows the original image and the singular values of the HSI data, column (b-2) provides the gradient maps among three dimensions, and column (c-1) plots the statistical histograms of gradient maps. It is evident that the original image exhibits low-rank characteristics, and its gradient maps demonstrate sparsity, indicating local smoothness in the HSI image.

Inspired by the presence of these two properties, it is natural to consider simultaneously modeling them in order to enhance recovery performance. An intuitive approach along these lines would involve combining low-rank regularization (e.g., nuclear norm) and TV regularization additively [30–33]. It makes the performance of this approach highly affected by the trade-off parameter imposed between the two regularizers. Generally, the low-rankness and smoothness are intercoupling in practical circumstances, each representing a type of information on the redundancy. Therefore, selecting appropriate parameters to achieve stable model performance is not always straightforward [34]. Another representative approach that combines low-rankness and smoothness is to incorporate TV regularization into the framework of low-rank decomposition [35–37]. Although this model has a low computational cost and avoids the need to tune the trade-off parameter between low-rankness and smoothness regularization terms, it is inevitably affected by the issue of unstable solving procedures due to inaccurate pre-specification of unknown rank.

To alleviate the above issues, Peng et al. [38] proposed a novel regularization term known as correlated total variation (CTV) in the matrix case, which was later extended to the tensor case by Wang et al. [34], resulting in tensor CTV (TCTV). The TCTV regularization effectively incorporates both prior information simultaneously. Indeed, as shown in Fig. 1(c-2), the T-SVD computation of gradient tensors reveals that only a few singular values are significant, indicating that the gradient tensors also possess low-rank structures. It indicates that, apart from sparsity, there consistently exists a strong correlation among gradient tensors, which finely conforms to the fact that priors always

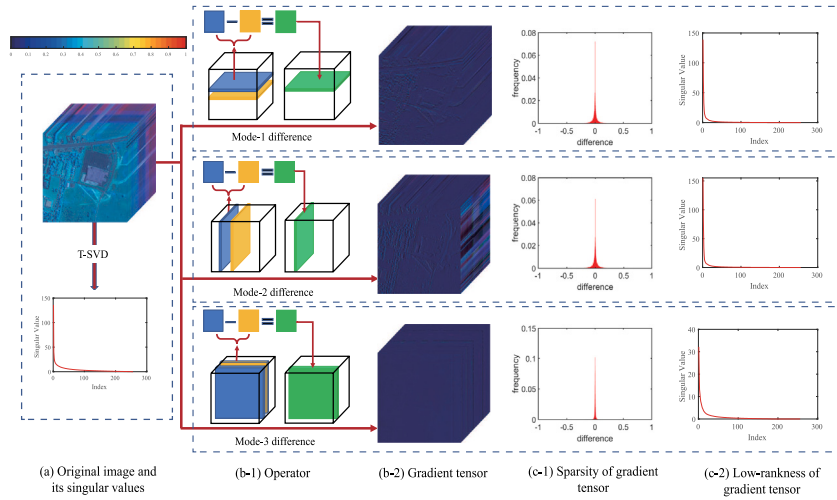


Fig. 1. Illustrations of the low-rank and local-smooth properties of HSIs. Column (a) shows the original image and the singular values of an HSI. Columns (b-1) and (b-2) provide the gradient maps of the HSI among three dimensions separately. Column (c-1) shows the statistical histogram of each gradient map. Column (c-2) shows the singular vector curve of each gradient map.

coexist jointly in natural visual tensor data. Mathematically speaking, the TCTV of tensor $\mathcal{X} \in \mathbb{R}^{n_1 \times n_2 \times n_3}$ can be modeled as the T-SVD on its gradient maps (refer to Definition 2.10). Peng et al. [38] and Liu et al. [39] have utilized CTV in solving robust principle component analysis (RPCA) problem and matrix CS problem respectively, where their corresponding CTV models demonstrate exact recovery theory under certain mild assumptions. Wang et al. [34] applied TCTV to the tensor RPCA and completion problems, also providing exact recovery guarantees for the two tasks. Recently, Liu et al. [40] utilized TCTV to solve the TCS problem and demonstrated that the error bound derived from TCTV is upper-bounded by the smaller one between those derived from TNN and TV seminorm. This suggests that the TCTV-based model can adaptively benefit from both properties.

As previously noted, the one-bit measurement model offers advantages in terms of hardware cost and sampling rate. This has been demonstrated to be applicable to the CS problem for low-rank tensors [17] and locally smooth tensors [22]. Given the prevalence of low-rank and locally smooth tensor data, as well as recent advancements in TCTV, we aim to investigate the applicability of TCTV for tensor recovery from binary measurements with improved performance. This paper aims to answer this question, and we summarize the contributions as follow.

- We propose a new model for the problem of TCS from binary measurements, which utilizes TCTV to simultaneously encodes both low-rank and smooth properties. We demonstrate that our proposed model yields an approximate estimate of the underlying low-rank and smooth tensor. Our method is robust against two common types of noise in binary measurements: bit flips and pre-quantization noise.
- We design an algorithm under the framework of ADMM [41] and prove its convergence to a global minimum of the proposed model through theoretical analysis. Numerical experiments conducted on HSIs, MSIs, and MRI data demonstrate that our method significantly improves both numerical and visual performance compared with TNN- or TV-based approaches alone. This conclusion is consistent with existing studies on TCS without binary quantization.

The remainder of this paper is organized as follows. Section 2 introduces notations, definitions, and lemmas that are useful. In Section 3, an optimization model based on TCTV is proposed along with corresponding theoretical guarantees. An algorithm based on ADMM with a convergence guarantee is presented in Section 4 to implement the proposed model. Numerical experiments are provided in Section 5, and finally, conclusions are drawn in Section 6.

2. Preliminaries

2.1. Notations

We first present some notations. We denote a scalar by a lowercase letter, e.g., x , a vector by a boldface lowercase letter, e.g., \mathbf{x} , a matrix by a boldface capital letter, e.g., \mathbf{X} , and a tensor by a boldface Euler script letters, e.g., \mathcal{X} . The i th element of vector \mathbf{x} is denoted as x_i , and the notation for matrices and tensors follows a similar convention. Let \mathbb{R} and \mathbb{C} denote the fields of real numbers and complex numbers, respectively. $[n]$ denotes the index set $\{1, 2, \dots, n\}$. For tensor $\mathcal{X} \in \mathbb{C}^{n_1 \times n_2 \times n_3}$, we use Matlab commands $\mathcal{X}(i, :, :)$, $\mathcal{X}(:, i, :)$, and $\mathcal{X}(:, :, i)$ to denote respectively the i th horizontal, lateral, and frontal slices, and denote its tubes as $\mathcal{X}(i, j, :)$ for any $1 \leq i \leq n_1$, $1 \leq j \leq n_2$. More often, we compactly denote $\mathcal{X}^{(i)}$ as the frontal slice $\mathcal{X}(:, :, i)$. For simplicity, we always set $n_{(1)} = \max\{n_1, n_2\}$ and $n_{(2)} = \min\{n_1, n_2\}$ throughout the paper. $\mathcal{T} = \mathcal{P} \Delta \mathcal{Q}$ denotes the frontal-slice-wise product (Definition 2.1 in [42]) between $\mathcal{P} \in \mathbb{C}^{n_1 \times n_2 \times n_3}$ and $\mathcal{Q} \in \mathbb{C}^{n_2 \times \ell \times n_3}$, i.e., $\mathcal{T}^{(i)} = \mathcal{P}^{(i)} \mathcal{Q}^{(i)}$, $i \in [n_3]$. The inner product of \mathcal{A} and \mathcal{B} is defined as $\langle \mathcal{A}, \mathcal{B} \rangle = \sum_{ijk} \mathcal{A}_{ijk} \mathcal{B}_{ijk}$. We denote the ℓ_1 norm and Frobenius norm of \mathcal{X} as $\|\mathcal{X}\|_1 = \sum_{ijk} |\mathcal{X}_{ijk}|$ and $\|\mathcal{X}\|_F = \sqrt{\sum_{ijk} |\mathcal{X}_{ijk}|^2}$, respectively. The above inner product and norms reduce to the vector or the matrix norms if \mathcal{X} is a vector or a matrix. For a matrix $\mathbf{X} \in \mathbb{C}^{n_1 \times n_2}$, its spectral norm and nuclear norm are defined as $\|\mathbf{X}\| = \max_{i \in [n_2]} \sigma_i(\mathbf{X})$ and $\|\mathbf{X}\|_* = \sum_i \sigma_i(\mathbf{X})$ respectively where $\sigma_i(\mathbf{X})$'s are the singular values of \mathbf{X} . Following the notation in [11], we define $\mathcal{X} \times_i \mathbf{U}$ as the mode- i product of tensor $\mathcal{X} \in \mathbb{R}^{n_1 \times n_2 \times n_3}$ with matrix $\mathbf{U} \in \mathbb{R}^{\ell \times n_i}$ ($i = 1, 2, 3$). For instance, computing $\mathcal{X} \times_2 \mathbf{U}$ is equivalent to performing the matrix-matrix multiplication $\mathbf{U} \mathbf{X}_{(2)}$, where $\mathbf{X}_{(2)}$ represents the mode-2 unfolding of tensor \mathcal{X} , initially forming an $\ell \times n_1 n_3$ matrix and then reshaping it into an $n_1 \times \ell \times n_3$ tensor.

2.2. Framework of T-SVD

We define $\bar{\mathcal{A}}$ by conducting a linear transform on \mathcal{A} along the 3rd dimension, i.e.,

$$\bar{\mathcal{A}} = L(\mathcal{A}) = \mathcal{A} \times_3 L, \quad (8)$$

where $L : \mathbb{C}^{n_1 \times n_2 \times n_3} \rightarrow \mathbb{C}^{n_1 \times n_2 \times n_3}$ denotes a linear transform specified by $L \in \mathbb{C}^{n_3 \times n_3}$. The inverse mapping of the linear transform L is given by $L^{-1}(\mathcal{A}) = \mathcal{A} \times_3 L^{-1}$. Throughout the paper, we assume

$$L^T L = L L^T = \mathcal{I}_{L_{n_3}}, \quad (9)$$

where $\ell > 0$ is a constant. We denote

$$\tilde{\mathcal{T}} := \text{bdiag}(\mathcal{T}) = \begin{bmatrix} \tilde{\mathcal{T}}^{(1)} & & & \\ & \tilde{\mathcal{T}}^{(2)} & & \\ & & \ddots & \\ & & & \tilde{\mathcal{T}}^{(n_3)} \end{bmatrix} \quad (10)$$

as the block diagonal matrix of $\tilde{\mathcal{T}}$, where $\tilde{\mathcal{T}}^{(i)}$ denotes the i th frontal slice of $\tilde{\mathcal{T}}$.

Let L be any invertible linear transform satisfying (9). We will now introduce the definition of a transform-based T-product and other related concepts.

Definition 2.1 (T-Product, [42]). The T-product of $\mathcal{A} \in \mathbb{R}^{n_1 \times n_2 \times n_3}$ and $\mathcal{B} \in \mathbb{R}^{n_2 \times \ell \times n_3}$, denoted as $\mathcal{C} = \mathcal{A} \star_L \mathcal{B}$, is defined such that $L(\mathcal{C}) = L(\mathcal{A}) \Delta L(\mathcal{B})$.

Definition 2.2 (Tensor Transpose, [42]). The tensor transpose of $\mathcal{A} \in \mathbb{R}^{n_1 \times n_2 \times n_3}$, denoted as \mathcal{A}^T , satisfies $L(\mathcal{A}^T)^{(i)} = (L(\mathcal{A})^{(i)})^T, i \in [n_3]$.

Definition 2.3 (Identity Tensor, [42]). Let $\mathcal{I} \in \mathbb{R}^{n \times n \times n_3}$ be such that each frontal slice of $L(\mathcal{I}) = \tilde{\mathcal{I}}$ is an $n \times n$ -sized identity matrix. Then the identity tensor is defined as $\mathcal{I} = L^{-1}(\tilde{\mathcal{I}})$.

Definition 2.4 (Orthogonal Tensor, [42]). If $\mathcal{Q}^T \star_L \mathcal{Q} = \mathcal{Q} \star_L \mathcal{Q}^T = \mathcal{I}$, then we say \mathcal{Q} is orthogonal.

Definition 2.5 (F-Diagonal Tensor, [42]). A three-order tensor is F-diagonal if all of its frontal slices are diagonal matrices.

With the aforementioned definitions, we are now prepared to present the L -based T-SVD in the subsequent lemma.

Lemma 2.1 (T-SVD, [42]). Any tensor $\mathcal{A} \in \mathbb{R}^{n_1 \times n_2 \times n_3}$ can be factorized as

$$\mathcal{A} = \mathcal{U} \star_L \mathcal{S} \star_L \mathcal{V}^T,$$

where $\mathcal{U} \in \mathbb{R}^{n_1 \times n_1 \times n_3}$, $\mathcal{V} \in \mathbb{R}^{n_2 \times n_2 \times n_3}$ are orthogonal tensors, and $\mathcal{S} \in \mathbb{R}^{n_1 \times n_2 \times n_3}$ is an F-diagonal tensor.

The transform based T-SVD has garnered considerable attention due to its advantages of closed multiplication operation, optimal representation, and the ability to achieve optimal approximation through truncation [42]. The definitions of tensor tubal rank, tensor spectral norm, and tensor nuclear norm related to the L -based T-SVD are presented below.

Definition 2.6 (Tensor Tubal Rank, [42]). The tensor tubal rank of $\mathcal{A} \in \mathbb{R}^{n_1 \times n_2 \times n_3}$, denoted as $\text{rank}_t(\mathcal{A})$, equal the number of nonzero singular tubes of \mathcal{S} , where \mathcal{S} comes from the transform-based T-SVD of $\mathcal{A} = \mathcal{U} \star_L \mathcal{S} \star_L \mathcal{V}^T$. Namely, $\text{rank}_t(\mathcal{A}) = \#\{i, \mathcal{S}(i, i, :) \neq \mathbf{0}\} = \max_{i \in [n_3]} (\text{rank}(\tilde{\mathcal{A}}^{(i)}))$.

Definition 2.7 (Tensor Spectral Norm, [23]). The tensor spectral norm of $\mathcal{A} \in \mathbb{R}^{n_1 \times n_2 \times n_3}$ is defined as $\|\mathcal{A}\| := \|\tilde{\mathcal{A}}\|$.

Definition 2.8 (Tensor Nuclear Norm (TNN), [23]). The tensor nuclear norm of $\mathcal{A} \in \mathbb{R}^{n_1 \times n_2 \times n_3}$ is defined as $\|\mathcal{A}\|_{\star_L} = \frac{1}{\ell} \|\tilde{\mathcal{A}}\|_{\star} = \sum_{i=1}^{n_3} \|(\mathcal{A} \times_3 L)^{(i)}\|_{\star}$.

The T-SVT operator, which performs tensor singular value thresholding, serves as the proximity operator for the TNN.

Lemma 2.2 (See [23]). Let $\mathcal{X} \in \mathbb{R}^{n_1 \times n_2 \times n_3}$ have the T-SVD decomposition $\mathcal{X} = \mathcal{U} \star_L \mathcal{S} \star_L \mathcal{V}^T$. The T-SVT operator defined under the L -based T-SVD is expressed as

$$D_{\tau}(\mathcal{X}) = \mathcal{U} \star_L \mathcal{S}_{\tau} \star_L \mathcal{V}^T, \quad (11)$$

where $\mathcal{S}_{\tau} = L^{-1}((L(\mathcal{S}) - \tau)_+)$, $\tau > 0$, and $t_+ = \max\{0, t\}$. For any $\rho > 0$ and $\mathcal{T} \in \mathbb{R}^{n_1 \times n_2 \times n_3}$, the T-SVT operator satisfies

$$D_{\rho}(\mathcal{T}) = \arg \min_{\mathcal{X}} \rho \|\mathcal{X}\|_{\star_L} + \frac{1}{2} \|\mathcal{X} - \mathcal{T}\|_F^2.$$

The following result presents a fundamental characteristic of tensor tubal rank in the transform-based T-SVD.

Lemma 2.3 (See [40]). Let $\mathcal{A} \in \mathbb{C}^{n_1 \times n_2 \times n_3}$ and $\mathcal{M} \in \mathbb{C}^{n_4 \times n_3}$, then we have

$$\text{rank}_t(\mathcal{A} \times_3 \mathcal{M}) \leq \text{rank}_t(\mathcal{A}). \quad (12)$$

Moreover, if \mathcal{M} has full column rank, the equality holds.

2.3. Total variation and correlated total variation

The total variation² of a tensor $\mathcal{A} \in \mathbb{R}^{n_1 \times n_2 \times n_3}$ is closely linked to its discrete gradients. Specifically, its gradient tensor along the j th ($j \in [3]$) mode can be mathematically defined as

$$\nabla_j \mathcal{A} := \mathcal{A} \times_j \mathbf{D}_{n_j}, \quad (13)$$

where $\mathbf{D}_{n_j} \in \mathbb{R}^{n_j \times n_j}$ is a differential matrix. In fact, the first $n_j - 1$ rows of \mathbf{D}_{n_j} are extracted from the first $n_j - 1$ rows of the row circulant matrix of $(-1, 1, 0, \dots, 0) \in \mathbb{R}^{n_j}$ and the final row is padded by a zero vector of length n_j .

Definition 2.9 (Total Variation (TV), [29]). The TV seminorm of $\mathcal{A} \in \mathbb{R}^{n_1 \times n_2 \times n_3}$ is defined as $\|\mathcal{A}\|_{\text{TV}} = \sum_{k=1}^3 \|\nabla_k \mathcal{A}\|_1$, where ∇_i denotes the differential operator along the i th dimension.

Recently, an interesting relation between the original tensor and its gradient maps was found by [34,40] as follows.

Lemma 2.4 (See [34,40]). Let $\mathcal{A} \in \mathbb{R}^{n_1 \times n_2 \times n_3}$, then for any $i \in [3]$, it holds that

$$\text{rank}_t(\mathcal{A}) - 1 \leq \text{rank}_t(\nabla_i \mathcal{A}) \leq \text{rank}_t(\mathcal{A}).$$

The finding indicates a correlation between the tubal rank of gradient maps and that of primordial tensors, implying that penalizing the tensor nuclear norm on its gradient maps, i.e., adopting TCTV as follows, can effectively capture the low-rankness of a tensor.

Definition 2.10 (Tensor Correlated Total Variation (TCTV), [34]). The TCTV of $\mathcal{A} \in \mathbb{R}^{n_1 \times n_2 \times n_3}$ is based on the T-SVD on its gradient maps via

$$\|\mathcal{A}\|_{\text{TCTV}} = \sum_{i=1}^3 \|\nabla_i \mathcal{A}\|_{\star_L},$$

where ∇_i denotes the differential operator along the i th dimension.

It has been demonstrated that minimizing the TCTV regularizer leads to a significant reduction in the TV regularizer [34,40]. Therefore, it is natural to employ TCTV as a joint regularization method for both low-rankness and smoothness.

3. Main theoretical results

To determine the required loss function in the model, we begin with a more general measurement setup. Drawing inspiration from one-bit CS [6], we assume that the response variables $y_i \in \{-1, 1\}$ are independently and randomly drawn such that

$$E(y_i | z_i) = \phi(z_i), \quad \forall i \in [m]. \quad (14)$$

² Here we mean the anisotropic total variation. Since the isotropic and anisotropic induced total variation seminorms are equivalent up to a constant factor [28], the definition of the isotropic total variation is omitted in this paper.

Here $z_i = \langle \mathcal{A}_i, \mathcal{X} \rangle$, $\mathcal{X} \in \mathbb{R}^{n_1 \times n_2 \times n_3}$ represents the tensor that needs to be recovered, and m follows the definition in (2). The function $\phi(\cdot)$ may be unknown or unspecified but must satisfy $-1 \leq \phi(z) \leq 1$. During the recovery stage, access to measurements y_i and sensing tensors \mathcal{A}_i is sufficient for recovering \mathcal{X} . Additionally, we introduce

$$E_{g \sim N(0,1)}(\phi(g)g) := \theta > 0 \quad (15)$$

to capture the relation between $\langle \mathcal{A}_i, \mathcal{X} \rangle$ and y_i . We have in [22] proved that

Lemma 3.1 (See [22]). *Following the definitions given by (14) and (15), it holds that $E[y_i \mathcal{A}_i] = \theta \mathcal{X}$ for each $i \in [m]$.*

As we only have access to the sign information of the random measurements in (2), it is impossible to reconstruct the magnitude of \mathcal{X} . Therefore, we will solely focus on recovering the direction of \mathcal{X} and assume $\|\mathcal{X}\|_F = 1$. It should be noted that Eq. (14) represents a generalized linear model in statistics, also referred to as the inverse link function. Standard one-bit measurement model thus becomes a special case of the model (14) with $\phi(\cdot) = \text{sign}(\cdot)$. In this situation, it is observed that $\theta = E(|g|) = \sqrt{2/\pi}$, which indeed attains the maximum relationship [6]. Since $E[y_i \langle \mathcal{A}_i, \mathcal{X} \rangle] = \theta \|\mathcal{X}\|_F^2 = \theta$ for each $i \in [m]$ by Lemma 3.1, it is expected that the potential optimal solution $\hat{\mathcal{X}}$ will also yield a high value for the objective function $\sum_{i=1}^m y_i \langle \mathcal{A}_i, \cdot \rangle / m$ subject to the constraint $\|\hat{\mathcal{X}}\|_F \leq 1$ according to the law of large numbers. Combining the relation function with the TCTV, we propose the following optimization model

$$\hat{\mathcal{X}} := \arg \min_{\|\mathcal{M}\|_F \leq 1} -\frac{1}{m} \sum_{i=1}^m y_i \langle \mathcal{A}_i, \mathcal{M} \rangle + \lambda \|\mathcal{M}\|_{\text{TCTV}}, \quad (16)$$

where λ denotes the regularization parameter. We will show that the optimal solution to model (16) yields an estimate of the underlying tensor from measurements (2). We mention that achieving exact recovery in one-bit CS is unattainable due to the fact that any unquantized measurement vector within an orthant of the measurement space will quantize to the same point as other vectors in that orthant, making it indistinguishable from them [2]. Nevertheless, we can provide an estimation of the upper bound for the recovery error.

Theorem 3.1. *Assume \mathcal{A}_i ($i \in [m]$) are independent sensing tensors populated by independent zero-mean Gaussian random variables with standard deviation 1. Let*

$$\lambda = c \sqrt{\frac{(n_1 + \theta^2)\ell \log(d)}{m}} \quad (17)$$

for constant $c := 1 + \sqrt{3}$, $d = (n_1 + n_2)n_3$, and ℓ defined as per (9). For any tensor $\mathcal{X} \in \mathbb{R}^{n_1 \times n_2 \times n_3}$, let the observations \mathbf{y} satisfy (14) and $\hat{\mathcal{X}}$ be the solution to model (16). Then with a probability at least $(1 - \frac{2}{(n_1 + n_2)n_3})^2$, it holds that

$$\frac{\|\mathcal{X} - \hat{\mathcal{X}}\|_F}{\sqrt{n_1 n_2 n_3}} \leq \frac{14\lambda}{\theta \sqrt{n_1 n_3}} = \mathcal{O}\left(\sqrt{\frac{\ell \log(d)}{mn_3}}\right). \quad (18)$$

We defer the proof process of Theorem 3.1 to the Supplementary Material.

Remark 1. Theorem 3.1 yields a highly general result, as the invertible linear transform L defined in (8) and (9) encompasses a broad spectrum of choices, including but not limited to the discrete Fourier transform (DFT), the discrete cosine transform (DCT), and the random orthogonal transform (ROM). Specifically, for DFT, (9) holds with $\ell = n_3$; whereas for both DCT and ROM, Eq. (9) holds with $\ell = 1$.

Remark 2. Theorem 3.1 offers a practical recommendation for selecting the regularization parameter λ of (16). Intuitively, when the sampling rate is high, the measurements contain more information,

thereby elevating the significance of the data fidelity term. In this case, Eq. (17) assigns the TCTV term a smaller weight due to $\lambda = \mathcal{O}(\sqrt{1/m})$. Conversely, a larger weight is attributed to the TCTV term.

Remark 3. It is worth noting that since $\|\mathcal{X}\|_\infty \leq 1$, the Frobenius norm of \mathcal{X} is on the same order as $\sqrt{n_1 n_2 n_3}$. Consequently, the relative error $\|\mathcal{X} - \hat{\mathcal{X}}\|_F / \|\mathcal{X}\|_F$ tends to be of order $\mathcal{O}(\sqrt{\ell \log(d)/(mn_3)})$. This means that the recovery performance can achieve arbitrary accuracy as long as the number of measurements (i.e., m) is sufficiently large. This provides an upper bound on the estimation error when we utilize the TCTV regularization in one-bit CS of tensors, providing a theoretical basis for further research on such issues. Moreover, as Theorem 3.1 is independent of the assumption regarding \mathcal{X} , it exhibits remarkable versatility across diverse application scenarios.

Except for the noiseless case of $\phi(\cdot) = \text{sign}(\cdot)$ with $\theta = \sqrt{2/\pi}$, Theorem 3.1 also covers the noisy one-bit measurements. In the presence of noise, the measurement model (2) can be modeled as

$$\mathbf{y} = \xi \odot \text{sign}(\mathfrak{M}(\mathcal{X}) + \mathbf{e}), \quad (19)$$

where \odot denotes componentwise multiplication, $\mathbf{e} \in \mathbb{R}^m$ are random noises before quantization, and $\xi \in \{-1, 1\}^m$ are populated by independent Bernoulli random variables satisfying $P(\xi_i = 1) = p$ and $P(\xi_i = -1) = 1 - p$, characterizing random bit flips in the measurements. Therefore, we derive a specific instance of model (14) with $\phi(z) = \xi_i \text{sign}(z + \tau_i)$. It is worth noting that $\phi(z) = E_{e_i}(E_{\xi_i}(y_i | z, e_i)) = 2(p - 1/2)(1 - 2P(e_i \leq -z))$, and the correlation coefficient $\theta = E(\phi(g)g)$ can be evaluated using integration by parts, which gives

$$\theta = 2(p - 1/2)E[\phi'(g)] = 4(p - 1/2)E[f(-g)] > 0, \quad (20)$$

where $g \sim N(0, 1)$ and $f(\cdot)$ denotes the density of e_i . Given concrete densities f , the specific value of θ can be calculated. For example, if e_i are normal random variables with mean zero and variance σ^2 , then

$$\theta = 2(p - 1/2)\sqrt{\frac{2}{\pi\sigma^2}}E(\exp(-g^2/(2\sigma^2))) = 2(p - 1/2)\sqrt{\frac{2}{\pi(\sigma^2 + 1)}}. \quad (21)$$

Applying Theorem 3.1 by plugging (21) into (17) indicates that recovering the tensor \mathcal{X} is still possible even when each measurement is flipped with probability nearly 1/2 and the noise level σ eclipses the magnitude of linear measurement. Eq. (18) suggests that a larger value of θ corresponds to a smaller recovery error. In the absence of noise, we can achieve the maximum with $\theta = \sqrt{2/\pi}$. However, in the presence of noise, higher bit flip rates (i.e., $1 - p$) or pre-quantization noise levels (i.e., σ) will result in smaller values of θ (see (21)), leading to greater recovery errors.

4. Algorithm

This section derives an algorithm for solving the TCTV-based model (16). It should be noted that (16) can be equivalently reformulated as

$$\begin{aligned} \min_{\mathcal{M}} & -\frac{1}{m} \sum_{i=1}^m y_i \langle \mathcal{A}_i, \mathcal{M} \rangle + \lambda \sum_{i=1}^3 \|\mathcal{G}_i\|_{\star_L} + I_{\{\|\mathcal{Z}\|_F \leq 1\}} \\ \text{s.t.} & \mathcal{Z} = \mathcal{M}, \mathcal{G}_k = \nabla_k \mathcal{M}, k \in [3], \end{aligned} \quad (22)$$

where $\mathcal{M} \in \mathbb{R}^{n_1 \times n_2 \times n_3}$ and the indicator function $I_{\{\|\mathcal{Z}\|_F \leq 1\}}$ is such that

$$I_{\{\|\mathcal{Z}\|_F \leq 1\}} = \begin{cases} 0, & \text{if } \|\mathcal{Z}\|_F \leq 1, \\ +\infty, & \text{if } \|\mathcal{Z}\|_F > 1. \end{cases}$$

We will now employ the Lagrange method to solve this problem. The augmented Lagrangian function for Eq. (22) is

$$\begin{aligned} \mathcal{L}(\mathcal{M}, \mathcal{Z}, \{\mathcal{G}_k, \Gamma_k | k \in [3]\}, \Lambda) \\ = -\frac{1}{m} \sum_{i=1}^m y_i \langle \mathcal{A}_i, \mathcal{M} \rangle + \lambda \sum_{i=1}^3 \|\mathcal{G}_i\|_{\star_L} + I_{\{\|\mathcal{Z}\|_F \leq 1\}} \end{aligned}$$

$$\begin{aligned}
& + \sum_{i=1}^3 \langle \Gamma_i, \mathcal{G}_i - \nabla_i \mathcal{M} \rangle + \langle \Lambda, \mathcal{Z} - \mathcal{M} \rangle \\
& + \frac{\rho}{2} \left(\sum_{i=1}^3 \|\mathcal{G}_i - \nabla_i \mathcal{M}\|_F^2 + \|\mathcal{Z} - \mathcal{M}\|_F^2 \right),
\end{aligned}$$

where $\Gamma_i (i \in [3])$ and Λ are all Lagrangian multipliers. It can also be reformulated as

$$\begin{aligned}
& \mathcal{L}(\mathcal{M}, \mathcal{Z}, \{\mathcal{G}_k, \Gamma_k | k \in [3]\}, \Lambda) \\
& = -\frac{1}{m} \sum_{i=1}^m y_i \langle \mathcal{A}_i, \mathcal{M} \rangle + \lambda \sum_{i=1}^3 \|\mathcal{G}_i\|_{\star_L} + I_{\{\|\mathcal{Z}\|_F \leq 1\}} \\
& + \frac{\rho}{2} \left(\sum_{i=1}^3 \left\| \mathcal{G}_i - \nabla_i \mathcal{M} + \frac{\Gamma_i}{\rho} \right\|_F^2 + \left\| \mathcal{Z} - \mathcal{M} + \frac{\Lambda}{\rho} \right\|_F^2 \right) + C,
\end{aligned} \quad (23)$$

where C is the only Lagrangian multipliers dependent squared item. We subsequently apply ADMM to optimize Eq. (23) and present our approach for solving the sub-problems related to each variable involved below.

(1) *Updating \mathcal{M}^{t+1}* : By taking the derivative of Eq. (23) with respect to \mathcal{M} and equating it to zero, we obtain the following equation

$$\left(\sum_{i=1}^3 \nabla_i^T \nabla_i + \mathbf{I} \right) (\mathcal{M}) = \frac{1}{m\rho_t} \sum_{i=1}^m y_i \mathcal{A}_i + \sum_{i=1}^3 \nabla_i^T (\mathcal{G}_i + \Gamma_i / \rho_t) + \mathcal{Z}^t + \Lambda^t / \rho_t, \quad (24)$$

where ∇_i^T denotes the transpose operator of ∇_i ³ and \mathbf{I} is the identity tensor of size $n_1 \times n_1 \times n_3$. Then, \mathcal{M}^{t+1} is such that (24) holds. The corresponding difference tensor of ∇_i for $i \in [3]$, denoted as \mathcal{D}_i , is defined as $\nabla_i(\mathcal{T}) = \mathcal{D}_i \star_L \mathcal{T}$ for any tensor \mathcal{T} , which can be obtained by $\mathcal{D}_i = \mathbf{I} \times_i \mathcal{D}_{n_3}$. Refer to [34] for more details. Following [43], we can apply multi-dimensional FFT, which diagonalizes \mathcal{D}_i , enabling to efficiently get the optimal solution of (24) based on the convolution theorem of Fourier transforms, i.e.,

$$\mathcal{M}^{t+1} = \mathcal{F}^{-1} \left(\frac{\mathcal{F} \left(\frac{1}{m\rho_t} \sum_{i=1}^m y_i \mathcal{A}_i + \mathcal{Z}^t + \Lambda^t / \rho_t \right) + \mathcal{H}}{1 + \sum_{i=1}^3 \mathcal{F}(\mathcal{D}_i^*) \odot \mathcal{F}(\mathcal{D}_i)} \right), \quad (25)$$

where $\mathcal{H} = \sum_{i=1}^3 \mathcal{F}(\mathcal{D}_i^*) \odot \mathcal{F}(\mathcal{G}_i + \Gamma_i / \rho_t)$ with \mathcal{D}_i^* being the tensor conjugate transpose [44] of \mathcal{D}_i , satisfying $L(\mathcal{D}_i^*)^{(k)} = (L(\mathcal{D}_i)^{(k)})^*$ for each $k \in [n_3]$, with $(L(\mathcal{D}_i)^{(k)})^*$ denoting the matrix conjugate transpose of $L(\mathcal{D}_i)^{(k)}$, $\mathbf{1}$ is a tensor with all entries being 1, and the division operation is componentwise as well.

(2) *Updating $\mathcal{G}_i^{t+1} (i \in [3])$* : By extracting all terms containing \mathcal{G}_i from (23), we obtain

$$\mathcal{G}_i^{t+1} = \arg \min_{\mathcal{G}_i} \frac{1}{2} \|\mathcal{G}_i - \nabla_i \mathcal{M}^{t+1} + \Gamma_i^t / \rho_t\|_F^2 + \frac{\lambda}{\rho_t} \|\mathcal{G}_i\|_{\star_L}.$$

The closed-form solution for this sub-problem is given by

$$\mathcal{G}_i^{t+1} = \mathcal{D}_{\lambda/\rho_t} (\nabla_i \mathcal{M}^{t+1} - \Gamma_i^t / \rho_t), \quad \forall i \in [3], \quad (26)$$

where $\mathcal{D}_\tau(\cdot)$ is defined as per (11).

(3) *Updating \mathcal{Z}^{t+1}* : By extracting all terms containing \mathcal{Z} from (23), we have

$$\mathcal{Z}^{t+1} = \arg \min_{\mathcal{Z}} \frac{\rho_t}{2} \|\mathcal{Z} - (\mathcal{M}^{t+1} - \Lambda^t / \rho_t)\|_F^2 + I_{\{\|\mathcal{Z}\|_F \leq 1\}},$$

which can be easily solved by projecting $\mathcal{M}^{t+1} - \Lambda^t / \rho_t$ to the set $\{\mathcal{Y} \in \mathbb{R}^{n_1 \times n_2 \times n_3} : \|\mathcal{Y}\|_F \leq 1\}$, i.e.,

$$\mathcal{Z}^{t+1} = (\mathcal{M}^{t+1} - \Lambda^t / \rho_t) / \max\{1, \|\mathcal{M}^{t+1} - \Lambda^t / \rho_t\|_F\}. \quad (27)$$

³ Since ∇_i is a linear operator, $\nabla_i(\mathcal{M})$ can be equivalent to $\mathcal{A}_i \text{vec}(\mathcal{M})$ with a matrix \mathcal{A}_i . Then, ∇_i^T means the operator equivalent to the transposed matrix \mathcal{A}_i^T .

Algorithm 1 ADMM for solving model (22)

Require: Measurement operator $\mathfrak{M} : \mathbb{R}^{n_1 \times n_2 \times n_3} \rightarrow \mathbb{R}^m$, binary measurements $\mathbf{y} \in \{\pm 1\}^m$.

Ensure: Approximation $\hat{\mathcal{M}} = \mathcal{M}^t$.

- 1: Initialize $\mathcal{M}^0, \mathcal{Z}^0, \Lambda^0, \mathcal{G}_i^0$, and Γ_i^0 for each $i \in [3]$ by padding them with zero elements, $\rho_0 = 10^{-5}$, $\rho_{\max} = 10^6$, $\text{tol} = 10^{-6}$, and $\psi = 1.1$.
- 2: **while** not convergence **do**
- 3: Update \mathcal{M}^{t+1} by (25).
- 4: Update \mathcal{G}_i^{t+1} by (26) for each $i \in [3]$.
- 5: Update \mathcal{Z}^{t+1} by solving (27).
- 6: Update multipliers Γ_i^{t+1} by (28) for each $i \in [3]$.
- 7: Update multiplier Λ^{t+1} by (29).
- 8: Update ρ_{t+1} by $\rho_{t+1} = \min(\psi \rho_t, \rho_{\max})$.
- 9: Check the convergence condition:
 $\|\mathcal{M}^{t+1} - \mathcal{M}^t\|_F / \max\{\|\mathcal{M}^t\|_F, 10^{-6}\} < \text{tol}$.
- 10: $t \leftarrow t + 1$.
- 11: **end while**

(4) *Updating $\Gamma_i^{t+1} (i \in [3])$ and Λ^{t+1}* : Based on the rule of ADMM, these multipliers are updated by

$$\Gamma_i^{t+1} = \Gamma_i^t + \rho_t (\mathcal{G}_i^{t+1} - \nabla_i \mathcal{M}^{t+1}), \quad \forall i \in [3], \quad (28)$$

and

$$\Lambda^{t+1} = \Lambda^t + \rho_t (\mathcal{Z}^{t+1} - \mathcal{M}^{t+1}). \quad (29)$$

Last, the penalty parameter ρ_{t+1} is updated by $\rho_{t+1} = \psi \rho_t$ with $\psi > 1$. We summarize the above procedure in Algorithm 1. The convergence of Algorithm 1 is guaranteed by the following theorem whose proof procedure is delayed to the Supplementary Material.

Theorem 4.1. *As t increases to infinity, the sequence $\{\mathcal{M}^t\}$ generated by Algorithm 1 converges to a global minimum of optimization problem (22).*

It is evident that the primary expense per iteration of Algorithm 1 lies in updating \mathcal{M}^{t+1} and $\mathcal{G}_i^{t+1} (i \in [3])$. The update of \mathcal{M}^{t+1} necessitates computing multidimensional FFT and inverse FFT of $n_1 \times n_2 \times n_3$ tensors, which possess a time complexity of $\mathcal{O}(n_1 n_2 n_3 \log(n_1 n_2 n_3))$. The update of $\mathcal{G}_i^{t+1} (i \in [3])$ involves computing the T-SVT operator. It is known that for any general linear transform L in (9), the time complexity of T-SVT is $\mathcal{O}(n_1 n_2 n_3^2 + n_{(1)} n_{(2)}^2 n_3)$. Therefore, the per-iteration complexity of Algorithm 1 is $\mathcal{O}(n_1 n_2 n_3 (n_3 + n_{(2)} + \log(n_1 n_2 n_3)))$. Note that for some specific linear transforms the per-iteration cost of T-SVT can be further reduced. For example, when L denotes the DFT, $L(\mathcal{X})$ can be calculated by performing FFT along the 3-rd dimension of $\mathcal{X} \in \mathbb{R}^{n_1 \times n_2 \times n_3}$, which costs $\mathcal{O}(n_1 n_2 n_3 \log(n_3) + n_{(1)} n_{(2)}^2 n_3)$ [12]. In this case, the per-iteration complexity of Algorithm 1 is $\mathcal{O}(n_1 n_2 n_3 (n_{(2)} + \log(n_1 n_2 n_3)))$.

5. Numerical experiments

This section comprises two parts. In the first part, we conduct experiments on synthetic data to facilitate the selection of regularization parameter λ in (16) and subsequently perform comparisons on various algorithms. In the second part, we compare our proposed methods with several competing ones across a range of datasets including HSIs, MSIs, and MRI images. All experiments are implemented on the platform of MATLAB (2016a) with AMD Ryzen 7 5800H 3.20-GHz CPU and 16 GB memory.

Prior to conducting experiments, we standardize the elements of all tensor data by dividing its infinity norm, thereby normalizing them within the range of $[-1, 1]$. Let SR denotes the sampling rate. While $\text{SR} \geq 1$ may not be of interest in traditional CS, it can prove to be highly practical in 1-bit (binary) systems capable of acquiring sign measurements at super-Nyquist rates [2]. This is because the conventional CS framework offers a means to alleviate the quantization bottleneck by

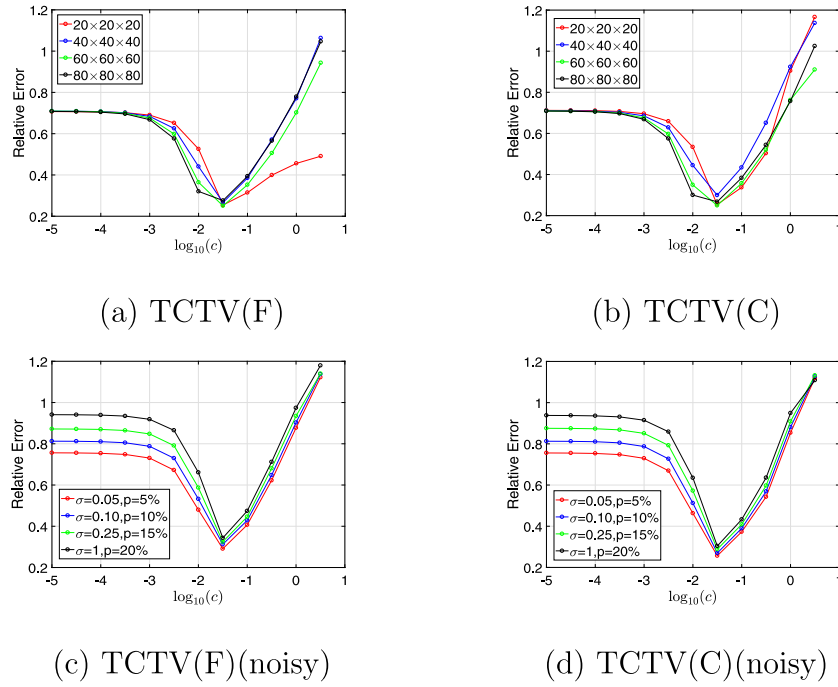


Fig. 2. Recovery errors obtained with different values of the constant c in (17). (a) and (b) show the results for TCTV(F) and TCTV(D) in the noiseless case, (c) and (d) shows the results for TCTV(F) and TCTV(D) in the noisy case.

reducing the analog to digital converter sampling rate, whereas the one-bit CS framework directly addresses this issue in the quantization domain by decreasing the number of bits per measurement.

To comprehensively evaluate the recovery performance across various applications, we first introduce some quantitative indicators. Specifically, for a tensor $C \in \mathbb{R}^{n_1 \times n_2 \times n_3}$ and its recovered result \hat{C} , the relative error is defined as $\|\hat{C} - C\|_F / \|C\|_F$. The peak signal-to-noise ratio (PSNR) and structural similarity (SSIM) [45] are two conventional spatial-based metrics, where higher PSNR and SSIM values indicate superior quality of the recovered images. We also employ erreur relative globale adimensionnelle de synthèse (ERGAS) and spectral angle mapper (SAM) [46] as spectral-based evaluation measures for HSIs. ERGAS quantifies the fidelity of the reconstructed HSI by calculating a weighted sum of mean square errors in each band, while SAM calculates the average angle between spectrum vectors of the recovered HSI and its corresponding reference at all spatial positions. For MRI data, we also utilize the high-frequency error norm (HFEN) [47] as a metric for evaluating the quality of edge and fine feature reconstruction.

5.1. Simulations

Before commencing the discussion, we shall elucidate the methodology for generating the requisite synthetic tensor $\mathcal{X} \in \mathbb{R}^{n_1 \times n_2 \times n_3}$ in our experiments. Drawing on Lemma 2.3, we posit that a tensor \mathcal{X} satisfying $\text{rank}_i(\mathcal{X}) = r$ ($r \leq \min\{n_1, n_2\}$) can be decomposed as $\mathcal{X} = \mathcal{T} \times_2 \mathbf{B}$ where $\mathcal{T} \in \mathbb{R}^{n_1 \times r \times n_3}$ is the coefficient tensor and $\mathbf{B} \in \mathbb{R}^{n_2 \times r}$ represents the base matrix. To ensure the local-smooth property of \mathcal{X} along with three directions, we require that each lateral slice $C(:, j, :)$ of C and each base vector $\mathbf{B}(:, j)$ of \mathbf{B} have local-smooth property. To this end, we adopt a method proposed in [40] which involves generating synthetic tensors through the following steps:

- Generate the coefficient tensor \mathcal{T} . We randomly select p initial points and set the remaining points allocated according to the distance to the initial point for each lateral slice. Then, each lateral slice is divided into p regions such that the entries of the same region are also the same, randomly generated from the standard normal distribution $\mathcal{N}(0, 1)$. To ensure $\text{rank}_i(\mathcal{X}) = r$, we

need $p \geq r$. Indeed, the bigger p is, the less smooth of each lateral slice of \mathcal{T} becomes.

- Generate the base matrix. For this purpose, we generate \mathbf{B} by independently drawing all its entries from $\mathcal{N}(0, 1)$ and then smooth each vector $\mathbf{B}(:, j)$ via a mean filter.

5.1.1. Parameter selection

We have analytically provided feasible choices for the regularization parameters λ in (16). However, the value of c suggested by Theorem 3.1 relies on certain mathematical techniques employed in the proof process, which prioritize compatibility with extreme data but may not always perform satisfactorily in practical applications. We can regard (17) as $\mathcal{O}(\sqrt{(n_{(1)} + \theta^2)\ell} \log(d)/m)$. It remains to determine the corresponding constant c through experimentation on synthetic data. Since the constant c do not depend on the structure of the tensor, the obtained parameter settings will be generalized.

We generate a synthetic tensor $\mathcal{X} \in \mathbb{R}^{n \times n \times n}$ using the aforementioned generation process. Specifically, we consider values of n within $\{20, 40, 60, 80\}$, with a tubal rank r equaling to $0.1n$ for each case. We utilize DFT and DCT as two specific cases of transform L and refer to the corresponding models as TCTV(F) and TCTV(C). Throughout the experiment, we maintain a fixed SR of 1. In the noiseless case, the relative errors for TCTV(F) and TCTV(C) are plotted in Fig. 2(a) and (b), respectively. We also introduce random bit flips and pre-quantization noise to the measurements in order to evaluate the parameter settings under noisy conditions. We set $n = 40$ and $r = 0.1n$. Each entry of binary measurements flips with a probability p , and the pre-quantization noises are generated from a mean zero Gaussian distribution with standard deviation $\sigma > 0$. Different levels of p and σ are tested in this experiment. The relative errors for TCTV(F) and TCTV(C) are respectively reported in Fig. 2(c) and (d). We can observe that $c = 10^{-1.5} \approx 3.2 \times 10^{-2}$ is always a proper choice for (17) whether in the presence or absence of noise. The experimental results provide further evidence to support the conclusion of Theorem 3.1, indicating that the proposed method performs well with an explicit regularization parameter for general tensor data. This setting can be maintained in the remaining experiments.

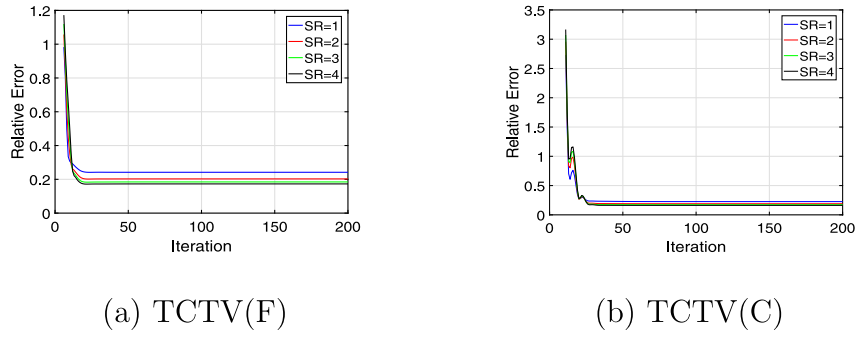


Fig. 3. Convergence of Algorithm 1. (a) shows the relative errors obtained by TCTV(F) with different iterations, and (b) shows the relative errors obtained by TCTV(C) with different iterations.

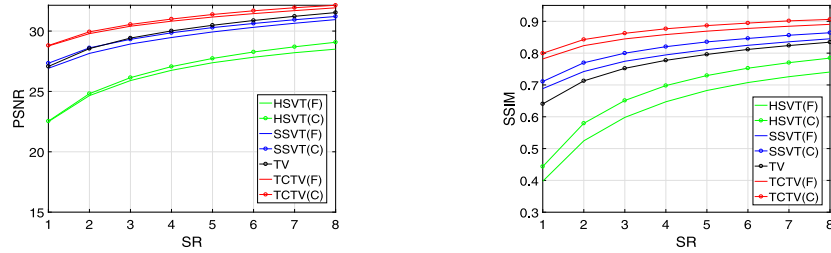


Fig. 4. PSNR and SSIM comparisons of different algorithms on synthetic data under different SRs.

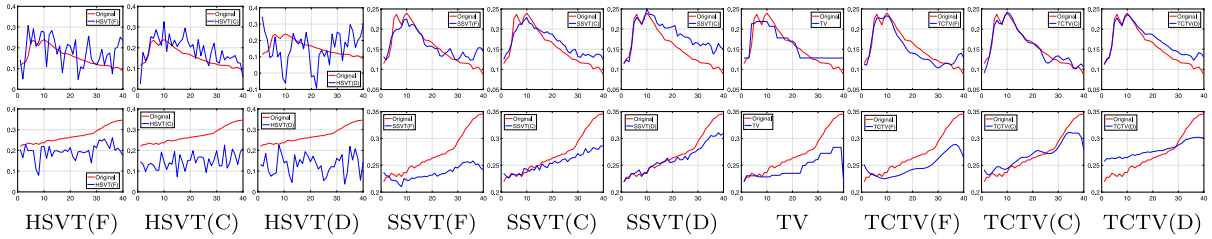


Fig. 5. Spectral signatures of both HSI datasets at SR = 4.

5.1.2. Algorithm convergence

In this part, we verify the convergence of Algorithm 1 with respect to the regularization parameter λ . Specifically, we randomly generate a $60 \times 60 \times 60$ tensor with tubal rank $r = 3$ and vary the SRs in $\{1, 2, 3, 4\}$, setting the maximum iteration as 200. The relative errors at different SRs are reported in Fig. 3(a) and (b), obtained by TCTV(F) and TCTV(C) respectively. The results show that both TCTV(F) and TCTV(C) converge within approximately 25 iterations, providing strong support for Theorem 4.1.

5.1.3. Comparisons on synthetic data

In this section, we compare the proposed methods with other competing approaches. Tensor hard singular value thresholding (HSVT) [17] and tensor soft singular value thresholding (SSVT) [22] are two recovery schemes for TCS from binary measurements using low-rankness. For the purpose of equitable comparisons, we also consider DFT and DCT as two specific examples of transform L for each scheme. We then designate the corresponding models as HSVT(F), HSVT(C), SSVT(F), and SSVT(C). We also compare with the TV seminorm based method, denoted as TV [22], which is a TV seminorm-based approach designed for CS of tensors exhibiting local smoothness from binary measurements. In the experiment, we randomly generate a $64 \times 64 \times 64$ synthetic tensor with tubal rank $r = 4$, and then test the recovery performance by calculating PSNR and SSIM indices. Fig. 4 illustrates the experimental results, demonstrating the superior performance of TCTV models across all SRs.

5.2. Applications

In this section, we apply the proposed method to various real-world applications in order to further evaluate its effectiveness. To simulate complex scenarios, binary measurements are utilized alongside simultaneous bit flips and pre-quantization noises. Specifically, each entry of binary measurements undergoes a flip with a probability of $p = 10\%$, while pre-quantization noises are generated from a Gaussian distribution with zero mean and standard deviation $\sigma = 0.10$.

5.2.1. Hyperspectral image recovery

HSIs are typically tensor data with both low-rank and smooth properties, as reported in previous studies [38]. HSIs are commonly acquired by airborne sensors or satellites and transmitted to ground stations on Earth for subsequent processing. Note that HSIs are of fairly large size due to the requirement of multi-spectral sampling over a wide spatial range. Consequently, effective techniques for compressing HSI data need to be developed considering the limited bandwidth of the link connection between satellites/aerospace platforms and ground stations. CS has been widely employed as an approach to address this challenge. Although recent advancements in CS technology have partially mitigated this issue [36,48], high-resolution quantization devices still suffer from bulky size and heavy load, thereby limiting their applicability in satellite or airborne scenarios. Our method based on 1-bit quantization exhibits reduced demands for quantization devices, thereby potentially facilitating the compression of HSIs.

Table 5.1

Four quantitative indices comparison of the proposed approaches over five competing methods on two HSIs at different SRs.

SR	Quality indices	Models									
		HSVT(F)	HSVT(C)	HSVT(D)	SSVT(F)	SSVT(C)	SSVT(D)	TV	TCTV(F)	TCTV(C)	TCTV(D)
HYDICE Urbanpart											
0.5	PSNR	19.807	20.230	20.439	27.612	27.915	28.046	28.361	29.362	29.361	30.335
	SSIM	0.1593	0.1600	0.1623	0.6773	0.6853	0.6907	0.7081	0.7455	0.7453	0.7858
	SAM	0.8403	0.7780	0.7339	0.1903	0.1612	0.1523	0.2163	0.1788	0.1894	0.1167
	ERGAS	34.6272	32.1458	31.1542	12.0560	11.6474	11.5067	11.2000	10.0860	10.1055	9.1334
1	PSNR	21.498	21.515	21.765	29.239	29.584	29.741	29.685	30.920	30.958	32.086
	SSIM	0.2237	0.2240	0.2307	0.7650	0.7745	0.7793	0.7764	0.8169	0.8171	0.8492
	SAM	0.6841	0.6237	0.5364	0.1604	0.1328	0.1232	0.1945	0.1483	0.1485	0.1004
	ERGAS	26.8866	25.3676	24.2357	10.0442	9.6550	7.5332	9.6476	8.4279	8.3966	7.5089
2	PSNR	24.148	23.176	23.783	30.970	31.309	32.191	31.143	32.543	32.551	34.446
	SSIM	0.3018	0.3038	0.3074	0.8337	0.8409	0.8664	0.8321	0.8686	0.8697	0.9093
	SAM	0.5391	0.4832	0.4308	0.1415	0.1143	0.1003	0.1742	0.1283	0.1243	0.0873
	ERGAS	21.4560	20.7092	19.3280	8.2733	7.9482	7.2579	8.1963	6.9954	6.9843	5.7939
4	PSNR	24.568	24.566	24.853	32.689	33.241	33.476	32.702	34.115	34.350	35.630
	SSIM	0.3934	0.3920	0.3984	0.8847	0.8937	0.8987	0.8770	0.9068	0.9115	0.9299
	SAM	0.4096	0.3659	0.3408	0.1253	0.1025	0.0905	0.1536	0.1137	0.0995	0.0818
	ERGAS	17.8287	17.7952	16.5822	6.8075	6.3860	6.2876	6.8762	5.8338	5.6810	5.0950
AVIRIS Moffett field											
0.5	PSNR	16.021	16.653	16.751	24.415	24.498	25.692	25.259	26.222	26.314	27.141
	SSIM	0.0885	0.0954	0.0985	0.5189	0.5127	0.5561	0.5585	0.6075	0.6171	0.6596
	SAM	0.7417	0.6777	0.6413	0.1776	0.1753	0.1354	0.1967	0.1478	0.1475	0.1111
	ERGAS	39.8491	36.2110	35.4020	13.1420	13.0030	11.8890	12.0037	10.9233	10.7946	9.9089
1	PSNR	18.039	18.689	18.982	25.650	25.836	27.208	26.442	27.569	27.761	28.678
	SSIM	0.1361	0.1464	0.1505	0.6067	0.6107	0.6542	0.6367	0.6924	0.7031	0.7387
	SAM	0.5788	0.5231	0.5044	0.1525	0.1487	0.1134	0.1739	0.1214	0.1184	0.0944
	ERGAS	29.8740	27.3074	25.3474	11.4839	11.2066	10.0459	10.5319	9.3731	9.1432	8.3261
2	PSNR	20.167	20.741	21.076	27.228	27.008	29.056	27.708	28.905	29.105	30.557
	SSIM	0.2076	0.2210	0.2301	0.6914	0.6959	0.7500	0.7044	0.7643	0.7722	0.8153
	SAM	0.4378	0.3915	0.3722	0.1318	0.1276	0.0950	0.1530	0.1032	0.0988	0.0799
	ERGAS	22.6768	20.9722	18.3667	9.9142	9.6098	8.1449	9.1762	8.0864	7.8668	6.7907
4	PSNR	22.186	22.560	22.984	28.472	28.761	30.120	29.082	30.299	30.556	31.632
	SSIM	0.3019	0.3180	0.3246	0.7639	0.7679	0.7946	0.7669	0.8209	0.8284	0.8484
	SAM	0.3237	0.2889	0.2624	0.1145	0.1088	0.0855	0.1340	0.0896	0.0841	0.0731
	ERGAS	17.6294	16.7291	15.7915	8.4593	8.1322	7.2211	7.8968	6.9458	6.7103	6.0520

We randomly selected two widely used HSIs: AVIRIS Moffett Field and HYDICE Urbanpart. After removing heavily polluted bands and cropping images, the resulting images were preprocessed to a size of $128 \times 128 \times 40$. Besides DFT and DCT, we also employ a unitary transform induced from the given tensor data inspired by [44]. Specifically, for the underlying tensor $\mathcal{X} \in \mathbb{R}^{n_1 \times n_2 \times n_3}$, we initially propose an estimator $\mathcal{B} \in \mathbb{R}^{n_1 \times n_2 \times n_3}$ using TCTV(C). Subsequently, we unfold \mathcal{B} into a matrix $\mathbf{B}^{(3)} \in \mathbb{R}^{n_3 \times n_1 n_2}$ along the third dimension. Let the SVD of $\mathbf{B}^{(3)}$ be denoted as $\mathbf{B}^{(3)} = \mathbf{U} \mathbf{S} \mathbf{V}^T$, where \mathbf{U}^T represents the desired orthogonal matrix for T-SVD induced from data. For simplicity, we refer to the corresponding algorithm as ‘TCTV(D)’. To comprehensively evaluate the performance of all approaches involved, we employed four quantitative quality indices: PSNR, SSIM, ERGAS, and SAM. Table 5.1 presents a comprehensive list of quality indices for all methods when SR is set to 0.5, 1, 2, and 4 respectively, with the best results highlighted in bold. As anticipated, the proposed TCTV based methods outperform most competing approaches in terms of quantitative metrics. Furthermore, the transformation induced from data exhibits better performance than both DFT and DCT. Fig. 5 plots the spectral curve⁴ of the pixel (50,50) in both HSIs obtained through different methods at SR = 4. It is evident that TCTV(D) produces a curve closer to the original compared to other methods, further validating its superiority. In Fig. 6, we present the tenth spectrum of each dataset along with the corresponding recovered images obtained using different methods at SR = 4.

⁴ HSI restoration is not only to recover a single band image more fully, but also to fully maintain the spectral curves of the substances. Here, the spectral curve is also called as spectral signature.

5.2.2. Multispectral image recovery

We present the outcomes of all competing techniques on three MSI datasets, namely Egyptian statue, Real and fake apple, and Clay, randomly selected from the CAVE MSI database [21] and reshaped to $128 \times 128 \times 31$ in this experiment. For quantitative comparison, Table 5.2 lists the PSNR and SSIM values obtained by different methods at different SRs. Meanwhile, Fig. 7 illustrates the fifth spectrum of each dataset and the corresponding recovered images generated by different approaches at SR = 4 for visual comparison. We have also observed that the TCTV-based methods demonstrate superior performance, with TCTV(D) yielding marginally better results compared to TCTV(F) and TCTV(C).

5.2.3. MRI data recovery

The primary obstacle hindering the clinical application of MRI stems primarily from stringent constraints on MRI speed, resulting in relatively lengthy examination times (with correspondingly high costs), limited spatiotemporal resolution and volumetric coverage, as well as sensitivity to respiratory motion. Given the high compressibility of MRIs, CS holds potential for effectively reducing acquisition time [49]. Recalling the cost-effectiveness and high sampling speed associated with 1-bit quantization, we aim to explore the potential application of our methodology for compressed sensing of MRI data.

We conducted experiments on two data sets. Data A is a publicly available myocardial perfusion MRI dataset obtained from [47], which was acquired using a saturation recovery FLASH sequence. Data B is a

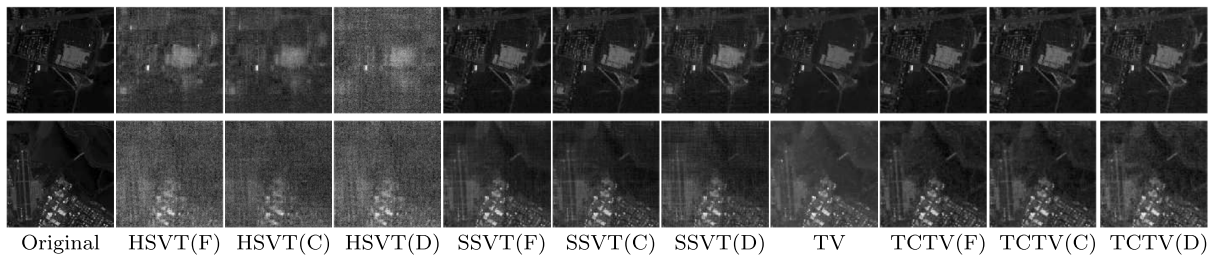


Fig. 6. Visual restoration effect display of all comparison methods on band 10 of both HSIs at SR = 4.

Table 5.2

PSNR and SSIM values comparison of the proposed approaches over five competing methods on three MSIs at different SRs.

SR	Quality indices	Models									
		HSVT(F)	HSVT(C)	HSVT(D)	SSVT(F)	SSVT(C)	SSVT(D)	TV	TCTV(F)	TCTV(C)	TCTV(D)
Egyptian statue											
0.5	PSNR	24.173	24.170	24.578	31.402	31.792	32.775	31.694	32.709	33.107	33.720
	SSIM	0.2543	0.2542	0.2578	0.7709	0.7667	0.7671	0.7770	0.7951	0.7938	0.8227
1	PSNR	27.641	27.410	27.876	32.251	33.810	34.271	32.823	34.596	34.064	35.896
	SSIM	0.4336	0.4385	0.4415	0.7823	0.8297	0.8308	0.7835	0.8482	0.8548	0.8652
2	PSNR	30.058	29.686	30.713	33.995	34.787	35.116	34.676	36.228	36.267	37.770
	SSIM	0.5957	0.5938	0.6009	0.7962	0.8300	0.8324	0.8152	0.8947	0.8984	0.9052
4	PSNR	31.705	31.557	31.925	36.022	36.741	37.374	36.843	37.783	38.200	39.578
	SSIM	0.7170	0.7210	0.7263	0.8637	0.8777	0.8810	0.8806	0.9290	0.9329	0.9366
Real and fake apple											
0.5	PSNR	23.574	24.567	25.293	30.488	31.429	31.926	31.612	33.824	34.560	36.014
	SSIM	0.2513	0.2870	0.3523	0.7366	0.7520	0.7544	0.7648	0.8375	0.8451	0.8723
1	PSNR	27.710	28.613	28.973	31.572	32.249	32.964	32.561	36.151	36.771	38.077
	SSIM	0.4478	0.4896	0.4921	0.7428	0.7605	0.7671	0.7716	0.8864	0.8873	0.9194
2	PSNR	31.050	31.634	32.073	33.453	34.197	34.831	34.419	38.065	38.666	39.973
	SSIM	0.6289	0.6549	0.6621	0.7830	0.7951	0.7987	0.8129	0.9215	0.9243	0.9434
4	PSNR	33.790	33.908	34.223	35.729	36.524	37.238	36.695	39.928	40.644	41.838
	SSIM	0.7647	0.7676	0.7701	0.8586	0.8692	0.8734	0.8802	0.9487	0.9524	0.9625
Clay											
0.5	PSNR	21.163	22.150	22.794	28.295	28.953	30.257	29.352	31.241	31.805	32.819
	SSIM	0.2153	0.2423	0.2487	0.6279	0.6356	0.6742	0.7027	0.7557	0.7568	0.7842
1	PSNR	25.277	26.296	26.573	29.371	29.876	31.166	30.110	33.583	34.063	35.391
	SSIM	0.3671	0.4131	0.4194	0.6442	0.6482	0.6535	0.7160	0.8092	0.8129	0.8363
2	PSNR	28.711	29.464	29.862	31.320	31.739	32.537	31.981	35.630	35.942	37.529
	SSIM	0.5371	0.5795	0.5841	0.6936	0.6988	0.7031	0.7293	0.8668	0.8672	0.8843
4	PSNR	31.654	32.076	32.761	33.592	34.048	34.880	34.213	37.459	37.803	39.459
	SSIM	0.6920	0.7265	0.7321	0.7899	0.7987	0.8010	0.8165	0.9150	0.9141	0.9231

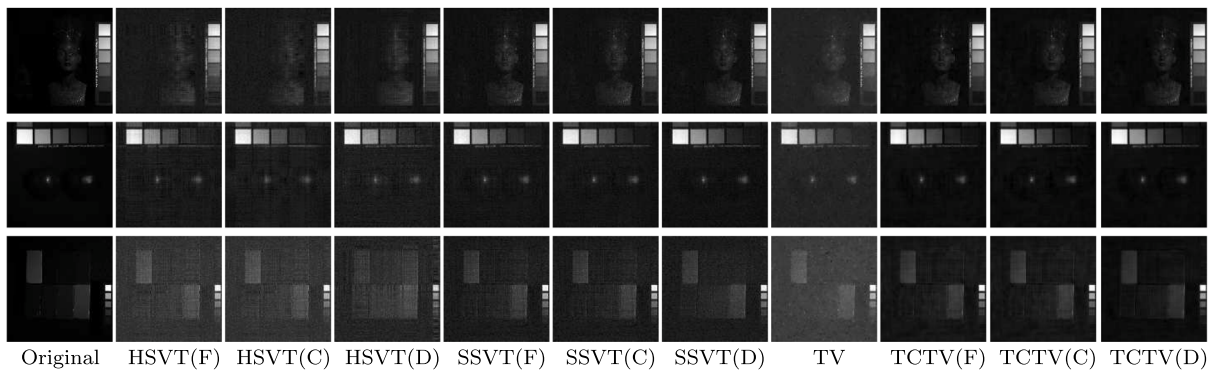


Fig. 7. Visual restoration effect display of all comparison methods on band 5 of Egyptian statue (upper), Real and fake apple (middle), and Clay (lower) at SR = 4.

cardiac cine MRI dataset distributed by the 2013 ISMRM Recon Challenge committee.⁵ In this experiment, we have resized the two datasets

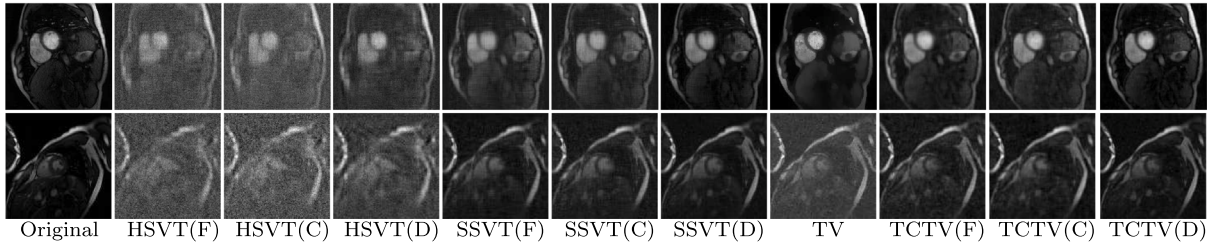
to $128 \times 128 \times 30$ and $128 \times 128 \times 24$ respectively. Table 5.3 presents quantitative indicators such as PSNR, SSIM, and HFEN at SRs of 0.5, 1, 2, and 4. Additionally, Fig. 8 illustrates the tenth frame of each dataset along with restored images obtained through various methods under SR = 1. We observe that TCTV based methods exhibit more competitive

⁵ <http://challenge.ismrm.org/node/66>.

Table 5.3

Comparison of the PSNR, SSIM, and HFEN values obtained by different methods on MRI at different SRs.

SR	Quality indices	Models									
		HSVT(F)	HSVT(C)	HSVT(D)	SSVT(F)	SSVT(C)	SSVT(D)	TV	TCTV(F)	TCTV(C)	TCTV(D)
Data A											
0.5	PSNR	19.168	19.166	19.773	26.327	26.699	27.427	27.291	28.605	29.301	29.763
	SSIM	0.1563	0.1575	0.1598	0.6300	0.6175	0.6397	0.7048	0.6823	0.6882	0.6942
	HFEN	1.0455	1.0423	1.0411	0.8193	0.7451	0.6817	0.6644	0.5778	0.5604	0.5328
1	PSNR	21.095	21.078	21.258	27.662	28.121	29.404	28.459	30.266	30.372	30.789
	SSIM	0.2213	0.2200	0.2256	0.6931	0.6929	0.6989	0.7453	0.7367	0.7495	0.7531
	HFEN	1.0075	1.0097	0.9234	0.6531	0.6008	0.5833	0.5410	0.4671	0.4618	0.4272
2	PSNR	22.918	22.911	23.305	29.015	29.501	31.014	29.736	31.266	31.423	31.827
	SSIM	0.3009	0.2992	0.2952	0.7507	0.7531	0.7652	0.7848	0.7885	0.7956	0.8017
	HFEN	0.9660	0.9726	0.8958	0.5143	0.4769	0.4200	0.4343	0.3852	0.3755	0.3118
4	PSNR	24.451	24.447	24.814	30.304	30.848	32.051	30.972	32.296	32.343	33.474
	SSIM	0.3924	0.3901	0.3941	0.7983	0.8039	0.8190	0.8172	0.8306	0.8330	0.8403
	HFEN	0.9200	0.9183	0.8594	0.4133	0.3829	0.3485	0.3544	0.3100	0.3098	0.2560
Data B											
0.5	PSNR	18.170	19.194	19.945	26.010	26.023	27.412	25.244	27.525	27.543	29.059
	SSIM	0.1433	0.1574	0.1591	0.5851	0.5793	0.5912	0.4844	0.5734	0.6038	0.6322
	HFEN	1.1009	1.0461	1.0221	0.6153	0.5693	0.4434	0.4622	0.4259	0.4352	0.4028
1	PSNR	19.628	21.082	21.378	27.594	27.906	29.393	27.536	29.409	29.227	30.374
	SSIM	0.1917	0.2203	0.2238	0.6687	0.6633	0.6922	0.5995	0.6740	0.7046	0.7233
	HFEN	1.0156	1.0068	0.9286	0.4766	0.4280	0.3848	0.3543	0.3294	0.3412	0.3045
2	PSNR	21.062	22.932	23.104	29.497	29.757	31.273	29.742	31.491	30.788	31.829
	SSIM	0.2484	0.3017	0.3089	0.7530	0.7474	0.7755	0.7138	0.7627	0.7870	0.7923
	HFEN	0.9330	0.9656	0.8502	0.3408	0.3176	0.2783	0.2625	0.2458	0.2554	0.2509
4	PSNR	22.273	24.450	24.741	31.207	31.560	32.674	32.001	32.953	32.212	33.469
	SSIM	0.3109	0.3926	0.4022	0.8188	0.8202	0.8484	0.8113	0.8373	0.8418	0.8266
	HFEN	0.8936	0.9387	0.8086	0.2607	0.2402	0.2083	0.1967	0.1874	0.1990	0.1889

**Fig. 8.** Visual restoration effect display of all comparison methods on frame 10 of both MRI datasets under SR = 1. Up: Data A; Down: Data B.

recovered details from the perspectives of both quantitative and visual results, providing further reinforcing evidence of the advantage of the proposed model.

6. Conclusion

This paper investigates the problem of recovering tensors with both low-rankness and local smoothness from binary measurements, proposing an efficient algorithm based on ADMM which guarantees global convergence. Experiments on both synthetic and real-world data sets have demonstrated the robustness and efficacy of the proposed model. Our findings may inspire further research using binary measurements by leveraging gradient maps to exploit the prevalent low-rank and local smoothness properties. For instance, we have explored the 1-bit low-rank tensor completion (LRTC) problem [26] and the quantized tensor robust principal component analysis (Q-TRPCA) problem [50] under the assumption of low rank. Whether TCTV can be applied to these problems to yield significant benefits remains to be explored.

CRedit authorship contribution statement

Jingyao Hou: Conceptualization, Funding acquisition, Investigation, Project administration, Supervision. **Xinling Liu:** Data curation, Validation, Writing – review & editing. **Hailin Wang:** Software, Writing – review & editing. **Ke Guo:** Validation, Writing – review & editing.

Declaration of competing interest

The authors declare that they have no known competing financial interests or personal relationships that could have appeared to influence the work reported in this paper.

Data availability

The data that has been used is confidential.

Acknowledgments

This research was supported in part by the National Natural Science Foundation of China (Grant Nos. 12201505, 12301594, 11801455, 11971238), in part by the Sichuan Science and Technology Program (Grant Nos. 2023NSFSC0060, 2023NSFSC1922), in part by the Open Project of Key Laboratory (Grant No. CSSXKFKTM202004), School of Mathematical Sciences, Chongqing Normal University, China, and in part by the Initiative Projects for Ph.D. in China West Normal University (Grant No. 22kE030).

Appendix A. Supplementary data

Supplementary material related to this article can be found online at <https://doi.org/10.1016/j.sigpro.2024.109480>.

References

- [1] D.L. Donoho, Compressed sensing, *IEEE Trans. Inform. Theory* 52 (4) (2006) 128–1306.
- [2] L. Jacques, J.N. Laska, P.T. Boufounos, R.G. Baraniuk, Robust 1-bit compressive sensing via binary stable embeddings of sparse vectors, *IEEE Trans. Inform. Theory* 59 (4) (2013) 2082–2102.
- [3] J. Konečný, H.B. McMahan, F.-X. Yu, P. Richtárik, A.T. Suresh, D. Bacon, Federated learning: Strategies for improving communication efficiency, 2016, arXiv preprint arXiv:1610.05492.
- [4] O.A. Hanna, Y.H. Ezzeldin, C. Fragouli, S. Diggavi, Quantization of distributed data for learning, *IEEE J. Sel. Areas Commun.* 2 (2021) 987–1001.
- [5] P.T. Boufounos, R.G. Baraniuk, 1-Bit compressive sensing, in: *Proc. 43rd Asilomar Conf. Signals Syst. Comput.*, 2008, pp. 16–21.
- [6] Y. Plan, R. Vershynin, Robust 1-bit compressed sensing and sparse logistic regression: A convex programming approach, *IEEE Trans. Inform. Theory* 59 (1) (2013) 482–494.
- [7] P. Xiao, B. Liao, Robust one-bit compressive sensing with weighted ℓ_1 -norm minimization, *Signal Process.* 164 (2019) 380–385.
- [8] J.Y. Hou, J.J. Wang, F. Zhang, J.W. Huang, One-bit compressed sensing via ℓ_p ($0 < p < 1$)-minimization method, *Inverse Problems* 36 (5) (2020) 055005.
- [9] T. Yang, M. Johannes, D. Sjoerd, C. Giuseppe, Plug-in channel estimation with dithered quantized signals in spatially non-stationary massive MIMO systems, 2023, arXiv preprint arXiv:2301.04641.
- [10] J.P. Xiong, Q.H. Tang, 1-Bit compressive data gathering for wireless sensor networks, *J. Sens.* 2014 (7) (2014) 177–183.
- [11] T.G. Kolda, B.W. Bader, Tensor decompositions and applications, *SIAM Rev.* 51 (3) (2009) 455–500.
- [12] C.Y. Lu, J.S. Feng, Y.D. Chen, W. Liu, Z.C. Lin, S.C. Yan, Tensor robust principal component analysis with a new tensor nuclear norm, *IEEE Trans. Pattern Anal. Mach. Intell.* 42 (4) (2020) 925–938.
- [13] M. Ding, T.Z. Huang, X.L. Zhao, T.H. Ma, Tensor completion via nonconvex tensor ring rank minimization with guaranteed convergence, *Signal Process.* 194 (2022) 108425.
- [14] F. Zhang, L.H. Yang, J.J. Wang, X. Luo, Randomized sampling techniques based low-tubal-rank plus sparse tensor recovery, *Knowl. Based Syst.* 261 (2023) 110198.
- [15] D. Banco, S. Aeron, W.S. Hoge, Sampling and recovery of MRI data using low rank tensor models, in: *Proc. 38th Annu. Int. Conf. IEEE Eng. Med. Biol. Soc.*, 2016, pp. 448–452.
- [16] S. Foucart, R.G. Lynch, Recovering low-rank matrices from binary measurements, *Inverse Probl. Imaging* 13 (4) (2019) 703–720.
- [17] J.Y. Hou, F. Zhang, H.Q. Qiu, J.J. Wang, Y. Wang, Y.D. Meng, Robust low-tubal-rank tensor recovery from binary measurements, *IEEE Trans. Pattern Anal. Mach. Intell.* 44 (8) (2022) 4355–4373.
- [18] M.E. Kilmer, C.D. Martin, Factorization strategies for third-order tensors, *Linear Algebra Appl.* 435 (3) (2011) 641–658.
- [19] X. Liu, J. Lu, L. Shen, Y. Xu, Multiplicative noise removal: nonlocal low-rank model and its proximal alternating reweighted minimization algorithm, *SIAM J. Imaging Sci.* 13 (3) (2020) 1595–1629.
- [20] C. Xu, X. Liu, J. Zheng, L. Shen, Q. Jiang, J. Lu, Nonlocal low-rank regularized two-phase approach for mixed noise removal, *Inverse Problems* 37 (8) (2021) 085001.
- [21] F. Yasuma, T. Mitsunaga, D. Iso, S.K. Nayar, Generalized assorted pixel camera: Post-capture control of resolution, dynamic range and spectrum, *IEEE Trans. Image Process.* 19 (9) (2010) 2241–2253.
- [22] J.Y. Hou, X.L. Liu, F. Zhang, J.J. Wang, T.W. Huang, Provable total variation regularized method for tensor compressed sensing from binary measurements, ResearchGate, available at <https://www.researchgate.net/profile/Jingyao-Hou>.
- [23] C. Lu, X. Peng, Y. Wei, Low-rank tensor completion with a new tensor nuclear norm induced by invertible linear transforms, in: *Proc. IEEE Comput. Vis. Pattern Recognit., CVPR*, 2019, pp. 5996–6004.
- [24] A. Aidini, G. Tsagkatakis, P. Tsakalides, 1-Bit tensor completion, *Electron. Imag.* 13 (2018) 1–6.
- [25] N. Ghadermarzy, Y. Plan, O. Yilmaz, Learning tensors from partial binary measurements, *IEEE Trans. Signal Process.* 67 (1) (2019) 29–40.
- [26] J.Y. Hou, F. Zhang, J.J. Wang, One-bit tensor completion via transformed tensor singular value decomposition, *Appl. Math. Model.* 5 (2021) 760–782.
- [27] J.F. Cai, W.Y. Xu, Guarantees of total variation minimization for signal recovery, *Inf. Inference* 4 (4) (2015) 328–353.
- [28] D. Needell, R. Ward, Stable image reconstruction using total variation minimization, *SIAM J. Imaging Sci.* 6 (2) (2013) 1035–1058.
- [29] D. Needell, R. Ward, Near-optimal compressed sensing guarantees for total variation minimization, *IEEE Trans. Image Process.* 22 (10) (2013) 3941–3949.
- [30] X. Li, Y. Ye, X. Xu, Low-rank tensor completion with total variation for visual data inpainting, *Proc. AAAI Conf. Artif. Intell.* 31 (1) (2017) 2210–2216.
- [31] D. Qiu, M.R. Bai, M.K. Ng, X.J. Zhang, Robust low-rank tensor completion via transformed tensor nuclear norm with total variation regularization, *Neurocomputing* 435 (2021) 197–215.
- [32] Y. Wang, Y.S. Han, K.D. Wang, X.L. Zhao, Total variation regularized nonlocal low-rank tensor train for spectral compressive imaging, *Signal Process.* 195 (2022) 108464.
- [33] Y.Y. Chen, T.T. Xu, X.J. Zhao, et al., Asymmetry total variation and framelet regularized nonconvex low-rank tensor completion, *Signal Process.* 206 (2023) 108901.
- [34] H.L. Wang, J.J. Peng, W.J. Qin, J.J. Wang, D.Y. Meng, Guaranteed tensor recovery fused low rankness and smoothness, *IEEE Trans. Pattern Anal. Mach. Intell.* 45 (9) (2023) 10990–11007.
- [35] T.Y. Ji, T.Z. Huang, X.L. Zhao, T.H. Ma, G. Liu, Tensor completion using total variation and low-rank matrix factorization, *Inform. Sci.* 326 (2016) 243–257.
- [36] Y. Wang, L. Lin, Q. Zhao, et al., Compressive sensing of hyperspectral images via joint tensor Tucker decomposition and weighted total-variation regularization, *IEEE Geosci. Remote Sens. Lett.* 14 (12) (2017) 2457–2461.
- [37] H.J. Zeng, X.Z. Xie, H.J. Cui, H.P. Yin, J.F. Ning, Hyperspectral image restoration via global l spatial-spectral total variation regularized local low-rank tensor recovery, *IEEE Trans. Geosci. Remote Sens.* 59 (4) (2020) 3309–3325.
- [38] J.J. Peng, Y. Wang, H.Y. Zhang, J.J. Wang, D.Y. Meng, Exact decomposition of joint low rankness and local smoothness plus sparse matrices, *IEEE Trans. Pattern Anal. Mach. Intell.* 45 (5) (2023) 5766–5781.
- [39] X.L. Liu, J.Y. Hou, J.J. Wang, Robust low-rank matrix recovery fusing local-smoothness, *IEEE Signal Process. Lett.* 29 (2022) 2552–2556.
- [40] X.L. Liu, J.Y. Hou, J.J. Peng, H.L. Wang, D.Y. Meng, J.J. Wang, Tensor compressive sensing fused low-rankness and local-smoothness, *Proc. AAAI Conf. Artif. Intell.* 37 (7) (2023) 8879–8887.
- [41] S. Boyd, N. Parikh, E. Chu, B. Peleato, J. Eckstein, Distributed optimization and statistical learning via the alternating direction method of multipliers, *Found. Trends Mach. Learn.* 3 (1) (2011) 1–122.
- [42] M.E. Kilmer, L. Horesh, H. Avron, E. Newman, Tensor-tensor algebra for optimal representation and compression of multiway data, *Proc. Natl. Acad. Sci. USA* 118 (28) (2021) e2015851118.
- [43] D. Krishnan, R. Fergus, Fast image deconvolution using hyper-Laplacian priors, in: *Proc. Neural Inf. Process. Syst.*, 2009, pp. 1033–1041.
- [44] G.J. Song, M.K. Ng, X.J. Zhang, Robust tensor completion using transformed tensor singular value decomposition, *Numer. Linear Algebra Appl.* 27 (3) (2020) e2299.
- [45] Z. Wang, A.C. Bovik, H.R. Sheikh, E.P. Simoncelli, Image quality assessment: From error visibility to structural similarity, *IEEE Trans. Image Process.* 13 (4) (2004) 600–612.
- [46] L. Wald, Data Fusion: Definitions and Architectures: Fusion of Images of Different Spatial Resolutions, Presses des l'Ecole MINES, Paris, 2002.
- [47] S.G. Lingala, M. Jacob, Blind compressive sensing dynamic MRI, *IEEE Trans. Med. Imaging* 32 (6) (2013) 1132–1145.
- [48] M. Golbabaee, P. Vandergheynst, Hyperspectral image compressed sensing via low-rank and joint-sparse matrix recovery, in: *Proc. 2012 IEEE International Conference on Acoustics, Speech and Signal Processing*, 2012, pp. 2741–2744.
- [49] J.P. Haldar, D. Hernando, Z.P. Liang, Compressed-sensing MRI with random encoding, *IEEE Trans. Med. Imaging* 30 (4) (2010) 893–903.
- [50] J.J. Wang, J.Y. Hou, Y.C. Eldar, Tensor robust principal component analysis from multi-level quantized observations, *IEEE Trans. Inform. Theory* 69 (1) (2023) 383–406.